Analytical and Experimental Investigation of the Feasibility of Accelerated Lifetime Testing of Materials Exposed to an Atomic Oxygen Beam

Final Report of

NASA Contract NAS8 - 37744

submitted on

June 11, 1993

submitted by

Royal Albridge, Alan Barnes, and Norman Tolk

Center for Molecular and Atomic Studies at Surfaces
Department of Physics and Astronomy
Vanderbilt University
Nashville, Tennessee

INTRODUCTION

The interaction of atomic particles with surfaces is of both scientific and technological interest. Past work emphasizes the measurement of high-energy sputtering yields. See Behrisch, R., editor, *Sputtering by Particle Bombardment I: Physical Sputtering of Single-Element Solids*, (Springer-Verlag, Berlin, 1981) for a survey of published sputtering yield data. Very little work utilized low-energy beams for which chemical and electronic effects can be important. Even less work has been carried out using well-defined low-energy projectiles. The use of low-energy, reactive projectiles permits one to investigate surface processes that have not been well characterized. As the energy of the projectile decreases, the collisional cascades and spikes, that are common for high-energy projectiles, become less important, and chemical and electronic effects can play a significant role (Sigmund, 1981).

Aspects of particle-surface interactions are of concern in several areas of technology. For example, the erosion, desorption, and glow of surfaces of spacecraft in orbit are important in the arena of space technology. The materials studied under this contract are of possible use on the exterior portions of the power generation system of Space Station Freedom. Under the original designs, Space Station Freedom's power generation system would generate potential differences on the surface as high as 200 volts. Ions in the plasma that often surround orbiting vehicles would be accelerated by these potentials leading to bombardment and erosion of the exposed surfaces. The major constituent of the atmosphere, approximately 90%, in the low earth orbit region is atomic oxygen. Since atomic oxygen is extremely reactive with most materials, chemical effects can arise in addition to the physical sputtering caused by the acceleration of the oxygen ions. Furthermore, the incident oxygen ions can remain embedded in the exposed surfaces, altering the chemical composition of the surfaces. Since the effective binding energy of a chemically altered surface can be quite different from that of the pure

substrate, the sputtering yield of a chemically altered surface is usually different also. The low-energy O^+ sputtering yield measurements, reported here, will help quantify the erosion rates for materials exposed to the low-earth orbit environment.

These measurements are of technological importance in another respect. In most surface analysis techniques, a surface is bombarded with ions, electrons or photons. Information concerning the structure of the surface and near-surface bulk, abundance of impurities and defects, as well as other surface properties are obtained either from the desorbed species or from the scattered projectiles. Because of their low penetration depth, low-energy ions provide an advantage over other techniques because they provide information that is more indicative of conditions on the surface rather than integrated effects arising from deeper in the bulk. A better understanding of the microscopic processes involved in these interactions is not only of basic scientific interest, but will also aid the scientific community by increasing the accuracy and usefulness of these surface analysis techniques.

EXPERIMENTAL METHODOLOGY

General

The erosion rate experiments described in this report were conducted in an ultra-high vacuum chamber with a base pressure of 1 x 10^{-9} Torr (1 x 10^{-8} Torr when running an ion beam). In these experiments, a low-energy ion beam was incident on a thin-film sample that covered a quartz-crystal microbalance. Bombardment of a surface with a low-energy reactive ion beam can simultaneously remove and add material to the surface of the substrate - sputtering of the substrate and incorporation of projectile particles into the substrate. Since the samples were thin films deposited on the surface of a 6 MHz AT-cut quartz crystal, the net mass change induced per incident ion was obtained by measuring the induced frequency shift of the quartz crystal. The current on a nickel grid was simultaneously measured to determine the number of ions incident on the sample. These measurements provided the information necessary to calculate the sputtering yield. Details concerning the apparatus and experimental procedure are discussed below.

The Ion Source and Accelerator

The ion beam is produced by a modified commercial Colutron ion source. The oven, where the gas is ionized and a plasma is maintained, is essentially a hot cathode type ion source (Figure 1). A quartz tube serves as the containment walls of the oven. At the back end of the oven, the gas inlet tube introduces the beam gas at pressures that are generally in the hundreds of mTorr region. The front of the oven is closed except for the 0.020 inch anode hole. This arrangement allows differential pumping between the inside of the oven and the rest of the ion source, where operating pressures are usually in the μTorr region.

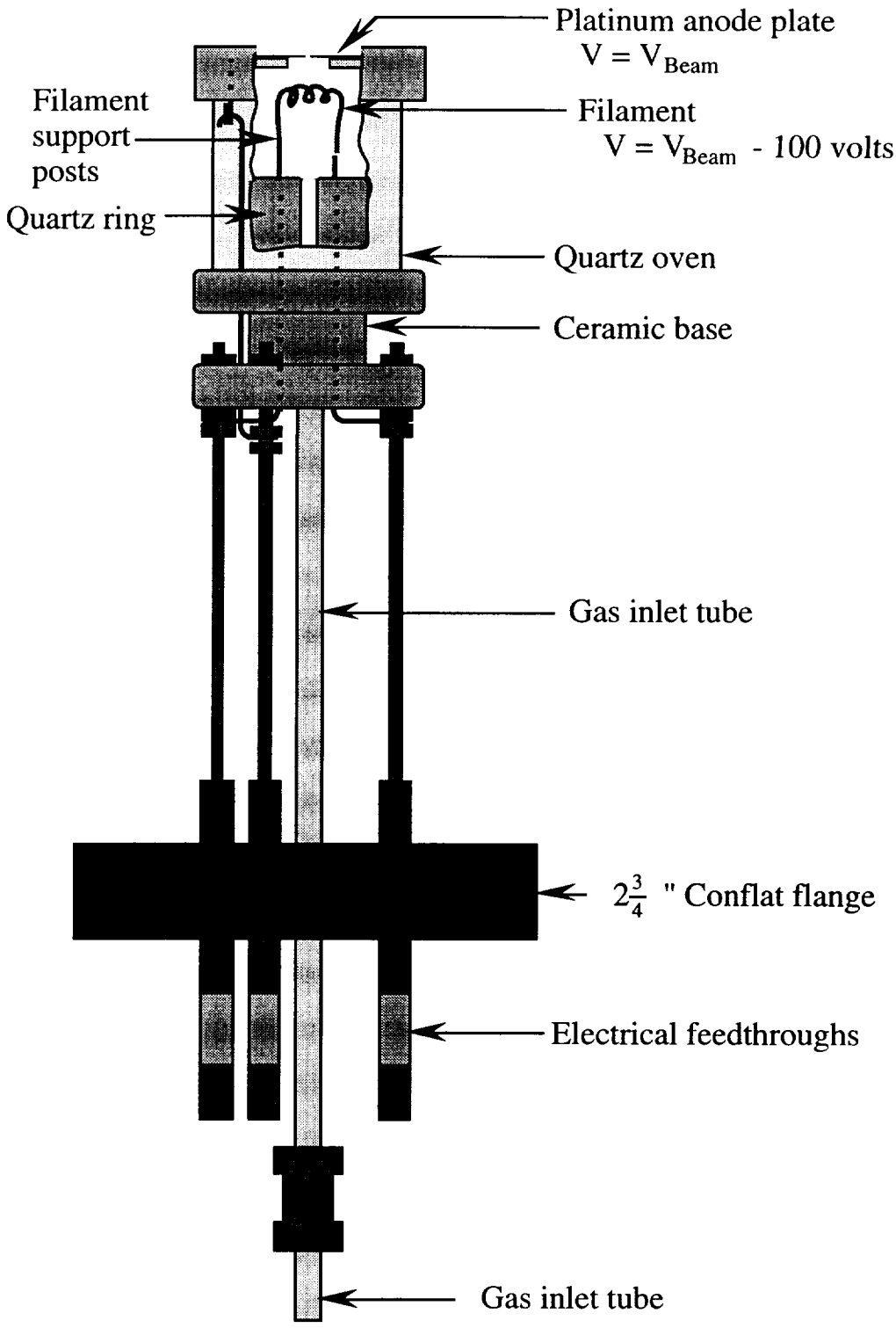

Figure 1. *The Colutron ion source.*

To create an ion beam, the gas atoms or molecules must first be ionized and even disassociated in cases where the introduced gas is a molecular species and atomic ions are desired, e.g. O^+ from O_2. A beam of electrons ionizes, and in some cases dissociates, the gas. The filament is heated by a current to a sufficient temperature to "boil" electrons from its surface. These electrons are then accelerated toward the anode by a 40- to 100-volt potential difference maintained between the anode and the filament. The positive ions that result from electron/atom collisions and ion/atom collisions form a plasma near the anode. Positive ions near the anode hole are then extracted by a negative 2-keV potential difference maintained between the extraction plate (see figure 2) and the anode.

The very corrosive, high temperature environment created in the oven when used to create an oxygen plasma necessitated the replacement of all the metal parts in the oven with more robust materials under these conditions. For the ion source, Colutron supplies tantalum anodes, alloy filament rods, and tungsten filaments. In a high temperature, oxygen- rich environment, the anodes oxidize and deform, the filament posts oxidize and coat the inside of the oven with metal oxides, and the tungsten filaments burn. The oxidation of the tungsten quenches the plasma and stops the discharge. To address these problems we replaced the anode and filament posts with similarly shaped platinum pieces. The platinum pieces are much less reactive with the oxygen and experience very little degradation even under these adverse conditions. Since the platinum filament posts become soft and move when heated, we designed a quartz ring with the appropriate holes to support the posts. The tungsten filament was replaced by an iridium ribbon coated with thorium oxide to reduce its work function. The iridium filaments last more than an order of magnitude longer than the tungsten in the oxygen environment.

The positive voltage applied to the anode determines the final beam energy (beam energy = anode voltage). The extraction plate is held 2 kV beneath the anode voltage to maintain a high extraction efficiency and to minimize the effects of space charge. The power supplies that control the beamline are then "floated" at the same potential as the extraction plate (Figure 2). All of the beam optics are referenced from this level and are

surrounded by a wire grid that is floated at the same potential in order to create a field-free region for the beam. Even though the ions are traveling with velocities defined by the 2-kV accelerating potential, they only have a potential energy, with respect to ground, that is equal to the voltage on the anode. We are therefore able to decrease the kinetic energy of the beam to the desired amount by placing two nickel grids (90 percent transmission, 70 lines per inch) in the path of the beam (Figure 4). The grids are perpendicular to the beam axis and parallel to each other. The first grid is held at the accelerating potential, while the second grid and the sample are grounded. The beam essentially doesn't "see" the first grid nor can it "see" the second grid until after it passes through the first grid. After passing through the first grid, the ions are decelerated. The kinetic energy of the ions is thus reduced to an energy determined by the voltage on the anode.

The extraction plate is mounted on the first section of an Einzel lens located immediately after the anode. The Einzel lens focuses the beam which is diverging as it emerges from the anode. As depicted in figures 2 and 3, the beam then goes through a set of vertical deflection plates for small steering corrections and a Wien filter for mass/velocity selection of a given charge state. The Wien filter allows selection of either an O^+ or an O_2^+ beam, for example, from the mixture that is extracted from the anode.

The primary purpose of the four sets of deflection plates that are encountered after the Wien filter is to remove high-energy neutrally charged particles from the beam. The neutral atoms or molecules arise from collisions during or immediately after extraction from the anode. The first set of plates is oriented in the vertical direction and serves to bend the beam to the right. The second and third sets of plates are positioned horizontally and are used to make slight corrections to the beam's vertical trajectory. The fourth set of plates, oriented in the vertical direction, bends the beam back to the left along a direction that is parallel to the original beam axis, but is offset 0.5 inch to the right. A copper block (1"x1"x1") with a 3/16" hole, angled at 1.3 degrees with respect to the original beam axis, is located between the second and third sets of plates. The copper block is

mounted on a plate that separates the high vacuum ion source from the ultra-high vacuum sample chamber. The small hole in the copper block allows for differential pumping by the two 200 liter/sec ion pumps located on the ultra-high vacuum side.

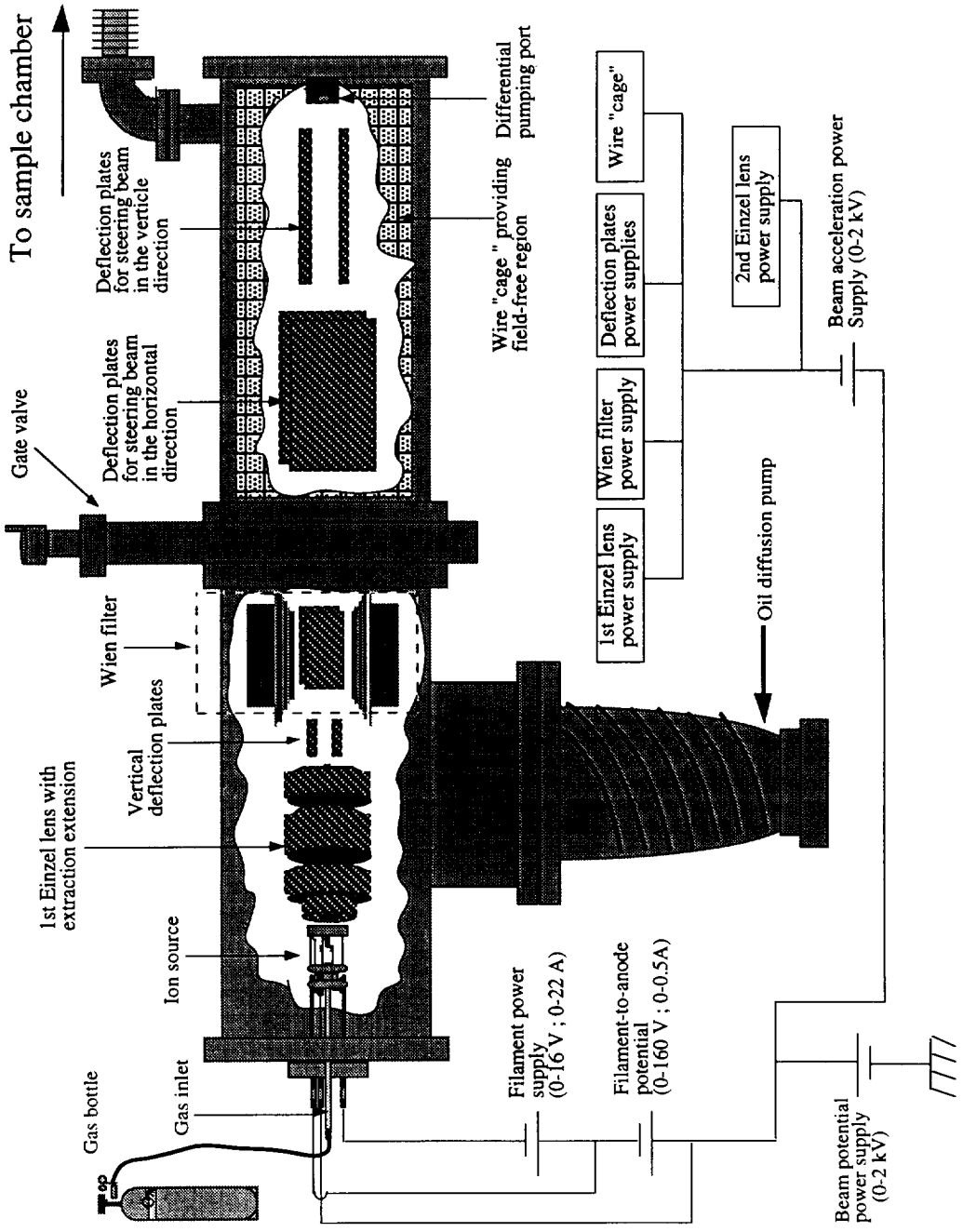

Figure 2. *Schematic diagram of high vacumm portion of beamline.*

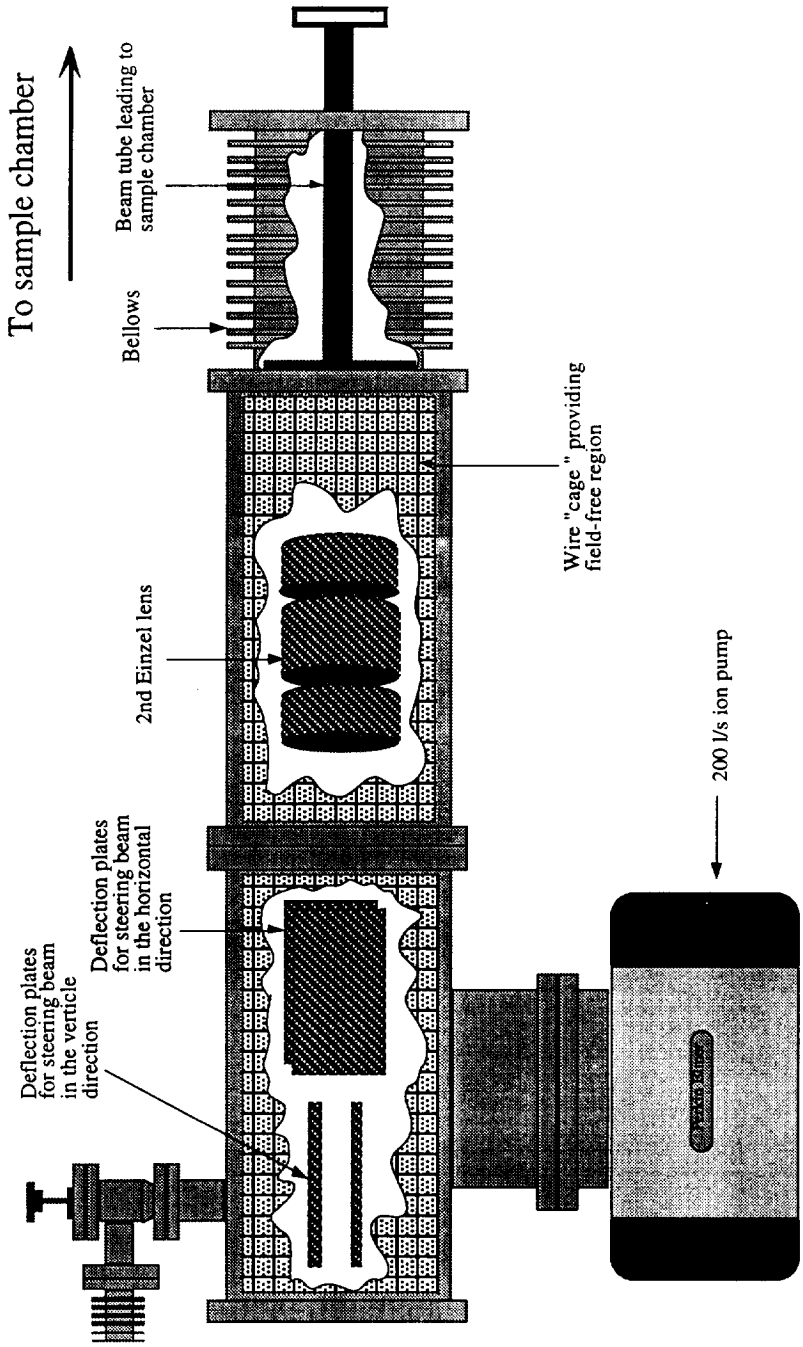

Figure 3. *Schematic diagram of ultra-high vacumm portion of beamline.*

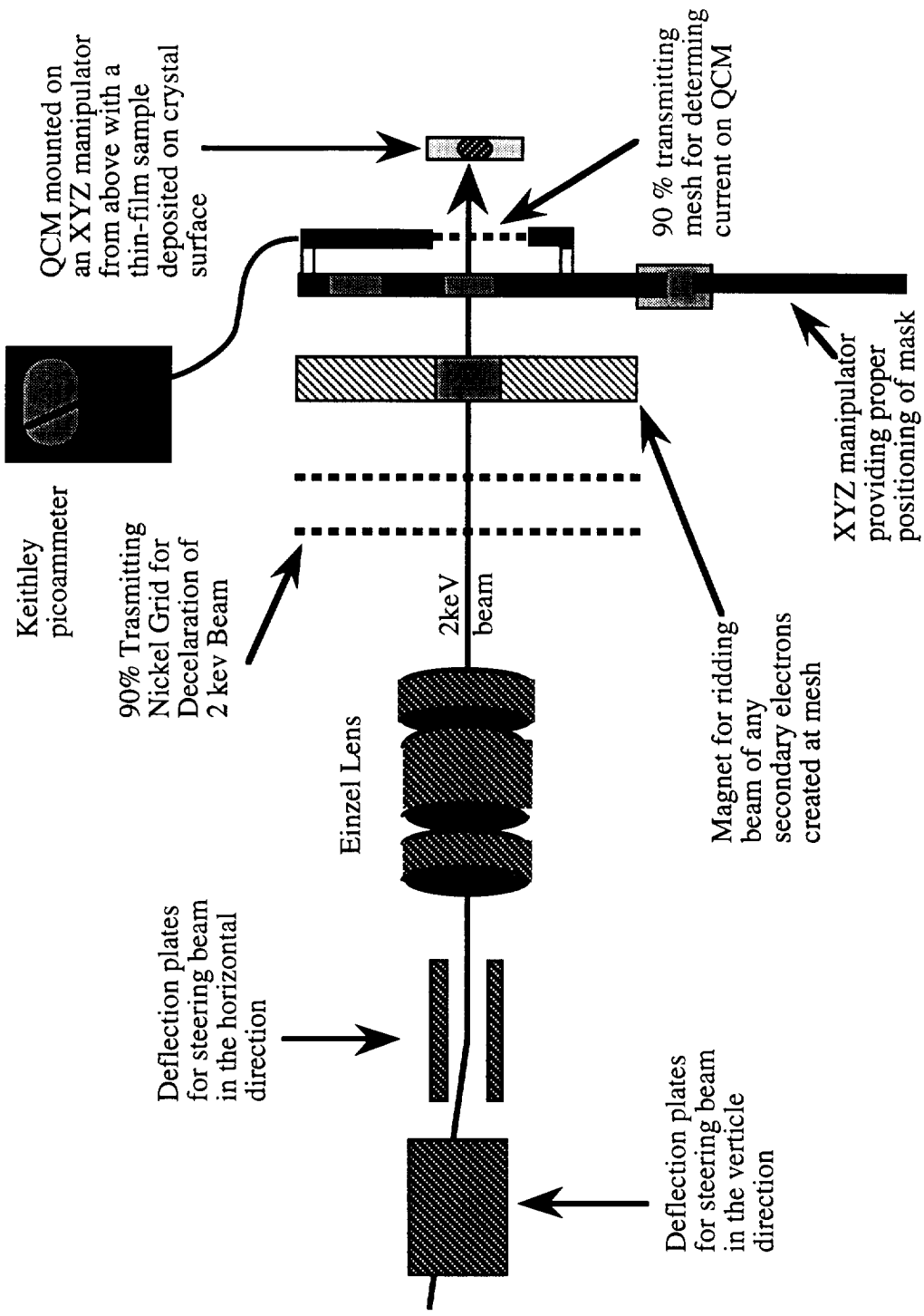

Figure 4. *Top view of final portion of beamline and sample chamber.*

A second Einzel lens, located after the fourth set of deflection plates, focuses the beam through the beam tube and onto the sample. The beam tube is floated at the accelerating potential and serves to shield the beam from the walls of the bellows, which

are grounded. Figure 4 shows that we have placed a permanent magnet between the last deceleration grid and the sample. When the ion beam strikes the grids, secondary electrons can be ejected from the grid. The electrons that are created at the first grid are then accelerated towards the target by the same potential difference that decelerates the ion beam. The permanent magnet diverts the electrons away from the target while bending the positive ion beam only slightly in the opposite direction.

Using the Quartz-crystal microbalance for Mass Loss Measurements

To measure erosion rates or sputtering yields, one needs to count the average number of particles emitted from the sample surface when a projectile ion strikes the sample at a given energy. This task is usually accomplished by measuring the total mass change of the sample when it is struck by a large known number of ions. From these data the total number of emitted atoms (or molecules) per incident particle is calculated. Because of its high sensitivity, we used a quartz-crystal microbalance (QCM) to measure the mass change. The samples were thin films sputtered or evaporatively deposited on the surface of the quartz crystals.

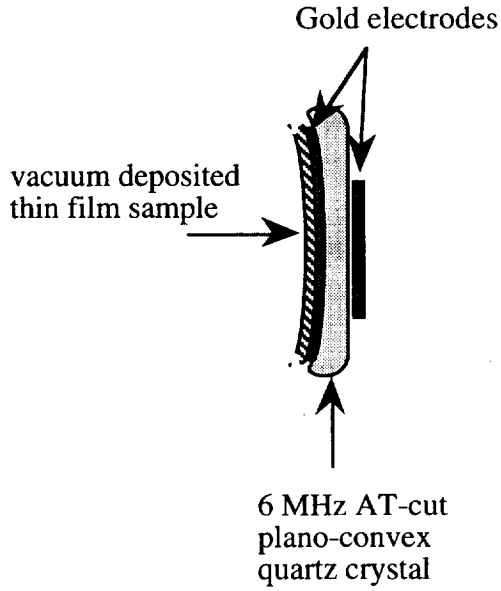

Figure 5. *Side view of the quartz crystal.*

QCM Theory and Operation

A quartz-crystal microbalance is comprised of a thin quartz wafer sandwiched between two metal electrodes, an oscillator circuit, and a circuit for measuring the resonant acoustic frequency of the crystal/thin-film system (see Figure 5). The oscillator circuit is utilized to apply a radio-frequency voltage across the electrodes which drives an acoustic mode in the piezoelectric quartz. This resonant acoustic mode is extremely sensitive to any mass loss or gain from the surface of the crystal. Sauerbrey was the first to methodically investigate the possibility of using a quartz crystal in the configuration described above to measure small mass changes (Ullevig and Evans, 1980). He noted that the mass change was proportional to the observed frequency shift; specifically, the magnitude of the mass change occurring on the surface of a quartz-crystal microbalance can be determined with the aid of Sauerbrey's relationship

$$\Delta f = -\frac{2 f_0^2 \Delta m}{A_e \sqrt{\rho_q \mu_q}} \tag{1}$$

where Δf is the observed frequency shift, f_0 is the parent frequency of the quartz crystal, Δm is the mass change, A_e is the active area of the crystal (i.e.. the area of the smallest electrode), ρ_q is the density of quartz (2.648 g cm^{-3}), μ_q is the shear modulus of the crystal (2.974 * 10^{11} dynes cm^{-2} for an AT-cut quartz crystal (Ward and Delawski, 1991)).

The constants in equation (1) can be grouped to obtain the relationship

$$\Delta f = \frac{-C_{total} \Delta m}{A_e} \tag{2}$$

where C_{total} is often called the sensitivity constant for the crystal. It should be noted that equation (2) is valid only if the induced frequency shift is small in comparison to the initial frequency of the crystal and the mass is added or removed uniformly across the active area of the crystal (Ullevig *et al.*, 1982).

If the mass change occurs over an area that is smaller than the active area of the crystal, the magnitude of C will depend on the area distribution over which the mass change occurs and the sensitivity function, $S(r)$, which describes the incremental frequency shift, df, induced by an incremental mass change, dm, at a given distance from the center of the active area. Stated differently, the sensitivity constant is merely a weighted summation of the sensitivity function across the area where the mass change occurs. Therefore when the mass change occurs uniformly across the total active area of the crystal, the sensitivity constant is

$$C_{total} = 2\pi \int_0^{r_e} rS(r)dr \quad \text{where} \quad S(r) = \frac{df(r)}{dm}. \qquad (3), (4)$$

The subscript "e" indicates that the entire electrode area is utilized. If the same amount of mass, Δm, were removed uniformly from a spot that is smaller than the active area, then a different frequency $\Delta f'$ would arise and the integration should be carried out over the spot area. Similar to equation (2), the new frequency would have the form:

$$\Delta f' = \frac{-C_{spot}\Delta m}{A_{spot}} \quad \text{where} \quad C_{spot} = 2\pi \int_0^{r_{spot}} rS(r)dr. \qquad (5), (6)$$

From an intuitive standpoint, it is not surprising that $S(r)$ is largest at the center of the crystal and decreases monotonically to the edge of the active area since the crystal is vibrating in a thickness shear mode. Several groups have measured the local vibration amplitudes of the quartz crystal - Sauerbrey (1964) used the modulation of a light beam, Wimmer *et al* (1984) made use of the speckle effect, and Mecea (1988) used a small rubber tipped wire to measure the vibration energy dissipation which he then converted to vibration amplitude. These measurements revealed that for an AT-cut quartz crystal, the amplitude of vibration is largest at the geometric center of the crystal's active area and a direct correlation can be made between the amplitude of the acoustic wave at a given concentric ring and the magnitude of the sensitivity function for that ring.

An Inficon XTC quartz crystal controller was used to drive the acoustic mode of the crystal and to measure the frequency shift induced when the ion beam removed mass

from the surface of the crystal. The controller automatically reports a mass change which corresponds to the frequency shift that would be induced if the mass were removed uniformly across the entire active area. However for this experiment, we chose to uniformly remove mass from a spot smaller than the electrode area in order to concentrate the small currents obtainable with our low-energy ion beam on the most sensitive area of the crystal. It was therefore necessary to relate the observed frequency shift, $\Delta f'$, to the frequency shift, Δf, that would have been induced by the same change in mass, Δm, if the mass were removed from the entire active area. To obtain this relationship, we divide equation (1) by equation (5) after replacing the sensitivity constants with the appropriate integrals from equations (3) and (6) to obtain

$$\frac{\Delta f}{\Delta f'} = \frac{\dfrac{2\pi\int_0^{r_e} rS(r)dr}{\pi r_e^2}}{\dfrac{2\pi\int_0^{r_{spot}} rS(r)dr}{\pi r_{spot}^2}}. \tag{7}$$

If we had the sensitivity function, $S(r)$, our task of relating $\Delta f'$ to Δf would be complete and we could determine the true mass loss Δm from that reported by the Inficon controller, $m_{reported}$, using the relationship

$$\Delta m = \Delta m_{reported}\frac{\Delta f}{\Delta f'}. \tag{8}$$

Since $S(r)$ is different for each coated crystal, it must be measured for each. In fact, Ullevig *et al.* (1982) showed that the integrated sensitivity constant is constant for a given crystal cut, but the sensitivity function will vary depending on the physical nature of the thin film on the crystal's surface. Furthermore, we only have the ability to measure a quantity, which we call $F(r)$, which is a convolution of the true sensitivity function with the finite area distribution from which the mass is removed. Measurement of the true sensitivity function would require removing mass from an infinitely small area, which is of course impossible with an ion beam of finite dimensions, while simultaneously measuring the induced frequency shift of the crystal. In fact, we determine $F(r)$ by

measuring a quantity that is proportional to *df/dm*. Fortunately the proportionality constant is not needed since *F(r)* is used in both the denominator and the numerator of the modified version of equation (7). The procedure for measuring *F(r)* will be discussed in a separate section. In the following section, we will show that the ratio of Δf to $\Delta f'$ given in equation (7) can also be computed using *F(r)*.

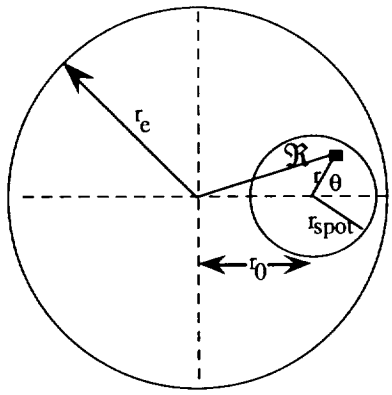

Figure 6. *Active area of crystal - radius r_e; spot radius r_{spot}.*

First, consider Figure 6 where the larger circle with radius r_e represents the active area of the crystal while the smaller area with radius r_{spot} represents the area of a hole in the mask that covers the crystal limiting the area of mass removal. As noted earlier, *F(r)* is actually a convolution of the true sensitivity function with the area from which the mass is removed, or

$$F(r_0) = \int_0^{2\pi} \int_0^{r_{spot}} r S(\Re) dr\, d\theta \tag{9}$$

where $\Re$ is the distance from the center of the active area to an infinitesimal area element of mass removal within the spot. As shown in Figure 6, it can be expressed as

$$\Re = \sqrt{r_0^2 + 2rr_0 \cos\theta + r^2}\,. \tag{10}$$

We noted earlier that *F(r)* is a convolution of the true sensitivity function with the finite area distribution from which the mass is removed. Closer inspection reveals that

the sensitivity constant can be computed using $F(r)$ if the integral is normalized by the area of the spot, i.e.

$$2\pi\int_0^{r_e} rS(r)dr = \frac{2\pi\int_0^{r_e} rF(r_0)dr}{\pi r_{spot}^2}. \tag{11}$$

Furthermore, Equation (10) shows that a special case exists when the spot is centered on the active area, i.e. when r_0 is zero.

$$F(0) = \int_0^{2\pi}\int_0^{r_{spot}} r_0 S(\Re)dr_0 d\theta = 2\pi\int_0^{rspot} rS(r)dr \tag{12}$$

Substituting equations (11) and (12) into equation (7) brings us to our objective - relating Δf to $\Delta f'$ using $F(r)$ instead of $S(r)$.

$$\frac{\Delta f}{\Delta f'} = \frac{\dfrac{2\pi\int_0^{r_e} rF(r)dr}{(\pi r_{spot}^2)(\pi r_e^2)}}{\dfrac{F(0)}{\pi r_{spot}^2}} = \frac{2\int_0^{r_e} rF(r)dr}{r_e^2 F(0)} \tag{13}$$

It is now possible to find the true mass change from the reported mass change when the mass is uniformly removed from a spot that is smaller than the active area of the crystal using the relationship

$$\Delta m = \Delta m_{reported}\frac{\Delta f}{\Delta f'}. \tag{14}$$

Measurement of the Convoluted Form of the Sensitivity Function

To measure $F(r)$, the QCM is first positioned so that the beam strikes the center of the active area while the area of mass removal is limited to the size of the hole in the mask. To insure uniform mass removal across the small spot area, the ion beam is rastered over an area slightly larger than the hole in the mask which defines the spot area. As described earlier, the number of ions striking the sample is recorded along with the *reported* mass change, $\Delta m'$ from the QCM controller While the beam and the mask remain stationary, the QCM is then moved so that the center of the small spot is

positioned a small radial distance from the center of the active area. Again the number of incident ions is recorded along with the reported mass change which should be smaller than the first since more mass is removed in this case from areas having smaller *S(r)*. This procedure is repeated - effectively moving the area of mass removal across the diameter of the active area. The magnitude of $\Delta m'$/(# incident ions) at a distance *r* from the center of the active area is equal to *F(r)* which is proportional to *df/dm* since the reported mass change is actually an interpretation, by the QCM controller, of the induced frequency shift. Furthermore, the normalization to the number of incident ions is equivalent to a mass normalization since an incident ion on the average always removes the same amount of mass regardless of the incident location. A plot of the results from this procedure produces a curve like the one in Figure 7 which is proportional to the true sensitivity function of the crystal *S(r)*.

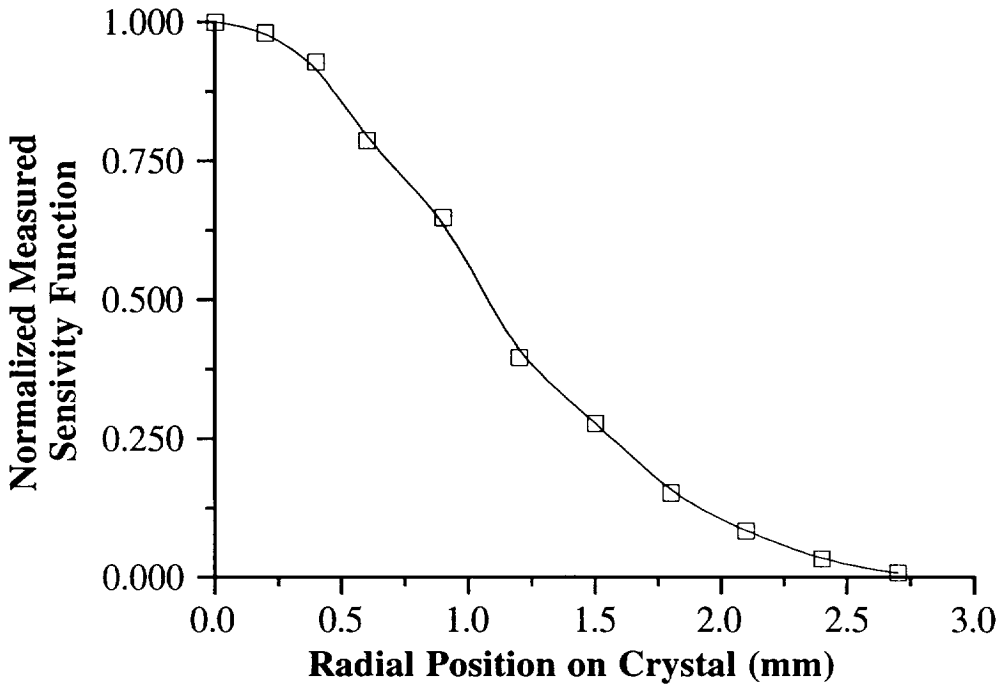

Figure 7. *The convoluted sensitivity function vs. the crystal radius.*

Sample Preparation

The gold electrodes on each side of the quartz are approximately 2500 Å thick and were evaporatively deposited by Inficon on a thin layer of chromium which bonds to the quartz better than gold (Roekel, LV., personal communication, February 19, 1992). The NASA Lewis Research Center prepared the aluminum and aluminum oxide samples by sputter deposition on the larger gold electrode as shown in Figure 5. The thickness of the aluminum oxide film was 1500 Å and that of the aluminum film was 2200 Å. (Vaughn, J., personal communication, February 19, 1992).

Prior to the erosion rate measurements, each sample was sputter-cleaned by a 2-keV argon-ion beam. A minimum of 40 Å of material was removed; and the argon bombardment was continued until the measured erosion rate of the sample became constant.

Data Acquisition

We determined the number of ions striking the sample by measuring the current in a grid located behind the 2-mm hole (see Figure 4). Prior to the erosion-rate experiments, we determined an energy-dependent conversion factor that relates the current incident on the sample surface to the current measured on the grid. (Corrections were made for secondary-electron emission.) An Inficon thin film rate monitor was used to drive the quartz crystal and extract the frequency shift needed for the determination of the mass change. A Macintosh IIci computer equipped with a National Instruments GPIB interface card was used to control the experiment, record the data, and perform the necessary calculations needed to extract the sputtering yield from the data.

To obtain the sputtering yield from the raw data, we first performed linear regression on the frequency data which are a function of the total ion dose. We then compared each measured frequency to the value predicted by the equation from the linear regression procedure. Measured frequencies that were more than 3 standard deviations from the predicted value were discarded and linear regression was performed again on the

remaining points. The slope obtained from the second linear regression procedure was then multiplied by the appropriate conversion factors to transform the frequency shift (corresponding to a specific mass change) to the corresponding number of sample atoms. That result was multiplied by another conversion factor to change the denominator to the number of incident ions, giving an uncorrected sputtering yield. This value was corrected by the factor of equation (14) to give our measured value of the sputtering yield.

EXPERIMENTAL RESULTS

The thicknesses of the films supplied by the NASA Lewis Research Center are shown in Table 1.

NASA Samples

Table 1. *Approximate film thicknesses of the NASA samples.*

NASA Samples	Approximate Film Thicknesses (Å)
Cu	800
SiO_X	1800
Al_2O_3	1500
Al	2200

Copper Sputtering Yield Results

For the copper sample, we measured the sputtering yields for low-energy O_2^+, O^+, N_2^+, and N^+ bombardment. The results are presented in Figure 8 and Table 2. The solid curves shown are second-order polynomial fits. Several low-energy sputtering measurements were made for N_2^+ on copper to determine the sputtering threshold. As can be seen in Table 2, the lowest energy at which a mass loss of the copper was measured was 60 eV. No measurable mass loss was observed for a 55 eV N_2^+ beam.

For oxygen bombardment of copper, a definite dependence of the measured sputtering yield on bombardment time was observed for both oxygen ion species. This time dependence is probably due to both an initial mass gain caused by the reactive incident particle and the true difference between the sputtering yields of the oxides formed on the surface layer and the sputtering yields of the pure metal. To quantitatively

address this issue, we devised a cleaning procedure that is discussed below. Preliminary experiments with the copper indicated that the time dependence of the O_2^+ and O^+ sputtering yields not only depends on bombardment time, but also on whether the copper surface was cleaned with an argon beam before oxygen bombardment. The copper samples were sputtered through to the gold substrate before more complete measurements could be made.

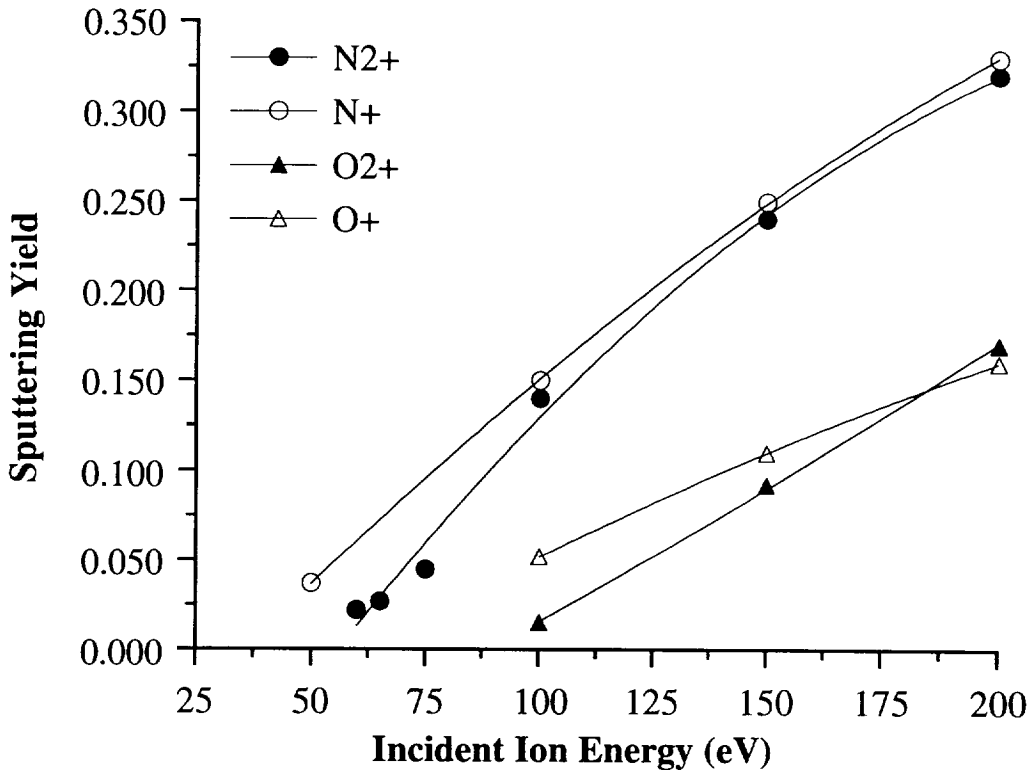

Figure 8. *Sputtering yield results as a function of energy for copper.*

Table 2. *Sputtering yield (average number of ejected atoms per incident ion) measurements for N_2^+, N^+, O_2^+, and O^+ on copper.*

Projectile Energy (eV)	N_2^+	N^+	O_2^+	O^+
50.0		0.037		
60.0	0.022			
65.0	0.027			
75.0	0.045			
100.0	0.14	0.15	0.015	0.052
150.0	0.24	0.25	0.092	0.11
200.0	0.32	0.33	0.17	0.16
400.0			0.57	

Silicon Oxide Sputtering Yield Results

For the silicon-oxide sample, we measured the sputtering yields for low-energy O_2^+, and O^+. The results are plotted in Figure 9 and listed in Table 3.

Because the exact compositions of the SiO_X samples are unknown, mass losses are reported instead of sputtering yields. Beam focusing and distortion was a problem for all measurements due to charging effects of the non-conductive sample. The mass losses are small for all bombardment energies studied. For example, a mass loss of 1.99×10^{-22} g for one 2 keV O_2^+ ion corresponds to a sputtering yield of only 0.42 if the sample was pure SiO_2 or 0.57 for pure SiO.

Table 3. *Mass loss measurements for O_2^+ and O^+ on SiOx.*

Projectile Energy (eV)	O_2^+ ($\times 10^{-22}$ g)	O^+ ($\times 10^{-22}$ g)
250.0	0.095	
500.0	0.38	0.35±0.05
1000.0	1.01	1.02±0.07
1500.0	1.41	1.35±0.26
2000.0	1.99	

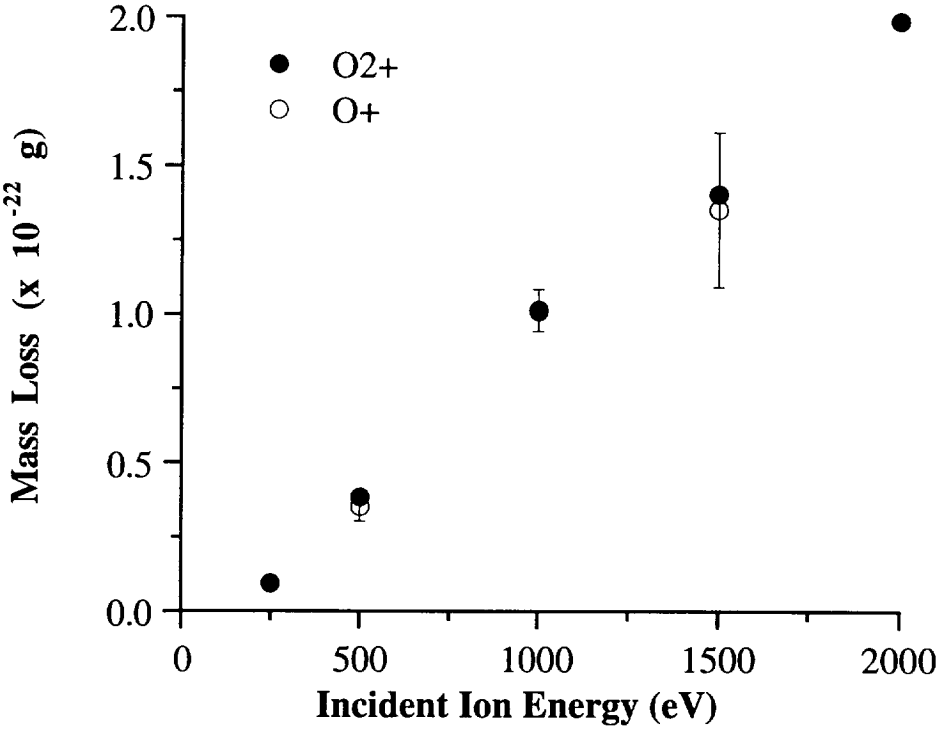

Figure 9. *Mass loss measurements as a function of energy for SiOx.*

Aluminum Oxide Sputtering Yield Results

For the aluminum-oxide sample, we measured the sputtering yields for low-energy O_2^+, O^+, N_2^+, and N^+ bombardment. The results are plotted in Figure 10 and listed in Table 4.

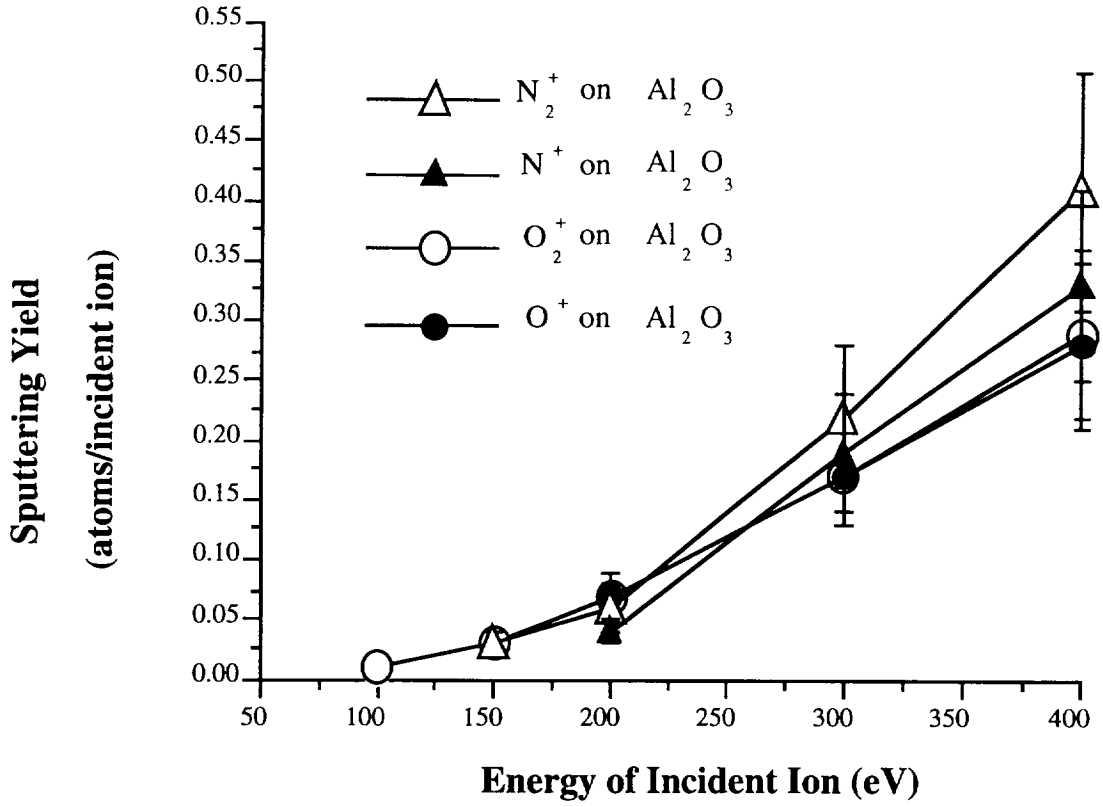

Figure 10. *Sputtering yields as a function of energy for aluminum oxide.*

Table 4. *Sputtering yield measurements on aluminum oxide sample.*

Projectile Energy (eV)	Projectile	$Y_{measured}$ (avg. # ejected atoms per incident ion)
2000	Ar^+	1.1 ± 0.3
400	N_2^+	0.41 ± 0.10
300	N_2^+	0.22 ± 0.06
200	N_2^+	0.06 ± 0.02
150	N_2^+	0.03 ± 0.01
400	N^+	0.33 ± 0.08
300	N^+	0.19 ± 0.05
200	N^+	0.04 ± 0.01
400	O_2^+	0.29 ± 0.07
300	O_2^+	0.17 ± 0.04
200	O_2^+	0.07 ± 0.02
150	O_2^+	0.03 ± 0.01
100	O_2^+	0.01 ± 0.004
400	O^+	0.28 ± 0.07
300	O^+	0.17 ± 0.04
200	O^+	0.07 ± 0.02

Based on what was learned from the Cu and SiO_x samples, a two step cleaning procedure was developed and used for all Al_2O_3 and Al samples. First, the sample surface was bombarded with a 2-keV Ar^+ beam until more than forty monolayers of material were removed and the erosion rate reached a constant value. After the argon beam was used to clean the sample and to measure the sensitivity function of the crystal, the sample was unavoidably exposed to the residual gases in the sample chamber (pressure $\approx 2x10^{-9}$ Torr) while the desired ion beam was being tuned. During this time, atoms and molecules from the vacuum adsorb on the surface of the sample. These atoms and molecules, H_2O, CO_2 etc., come from background gases in the sample chamber that stick to the surface during the time between the Ar^+ cleaning and the bombardment with the beam of interest. In the second stage of the cleaning process, the ion beam to be used for the actual sputtering yield measurement was first used to remove several monolayers of material from the sample while the sputtering rate was simultaneously measured. The second stage of cleaning was terminated when the measured sputtering yield became constant, indicating that the adsorbed species on the surface were removed. At the beginning of both cleaning processes, the mass change per incident ion is slightly larger than the final value. This difference occurs because the weakly bound surface adsorbates are much easier to sputter from the surface than are the aluminum-oxide molecules. The sputtering yields reported represent the constant values obtained after the surface impurities were removed.

Aluminum Sputtering Yield Results

The aluminum samples were cleaned by the procedure described above. During this procedure, it soon became apparent that the cleaning process was even more critical than it had been for the aluminum oxide. Again at the beginning of the cleaning process, the sputtering yield was larger than the final value. However, an intermediate stage was also observed in which the sputtering yield was smaller than the final constant value reached. Since the samples were exposed to air for several months before the experiment,

the top layers of the aluminum were at least partially composed of aluminum oxide. The measured results of the final constant sputtering yield reached are plotted in Figure 11 and listed in Table 5.

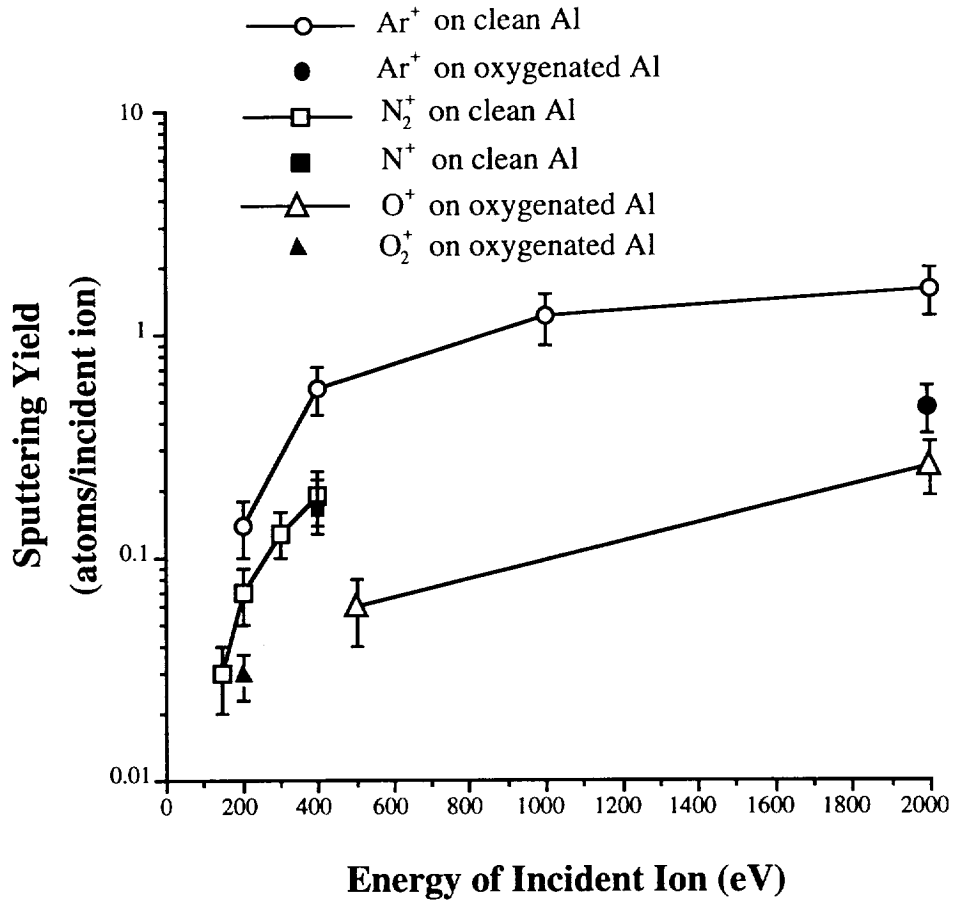

Figure 11. *Semilog plot of sputtering yield as function of energy for aluminum.*

The term "oxygenated aluminum" is used to describe the aluminum surface after bombardment with an oxygen beam. As will be discussed in greater detail below, the mass of the aluminum sample actually increases when the clean aluminum surface is bombarded with a low-energy ionic oxygen beam; and then the sample stops gaining mass and starts losing mass. The oxygen is obviously embedded into the surface and near-surface bulk of the initially pure aluminum. For oxygen bombardment of aluminum, we report the sputtering yield of the chemically altered surface obtained when the amount of mass loss per incident ion reaches a constant value. We are using the term

"oxygenated aluminum" to describe the surface of the aluminum sample after it has been exposed to a sufficiently large dose of oxygen that an equilibrium condition is reached and a net mass loss per incident oxygen ion is observed or no mass gain is observed. To investigate the effects of the chemically altered surface on the sputtering yield of a non-reactive bombarding species, a 2-keV Ar^+ run was conducted on the oxygenated surface. The measured sputtering yield was much smaller than we had previously measured for 2-keV Ar^+ on the pure aluminum surface.

Table 5. *Sputtering yield measurements on aluminum sample.*

Projectile Energy (eV)	Projectile	Sample	$Y_{measured}$ (avg. # ejected atoms per incident ion)	$Y_{literature}$ (avg. # ejected atoms per incident ion)
2000	Ar^+	Al	1.6 ± 0.4	
2000	Ar^+	oxygenated Al	0.48 ± 0.12	
1000	Ar^+	Al	1.2 ± 0.3	2.0[1]
400	Ar^+	Al	0.69 ± 0.17	0.8[2]
200	Ar^+	Al	0.14 ± 0.04	0.35[2]
400	N_2^+	Al	0.19 ± 0.05	
300	N_2^+	Al	0.13 ± 0.03	
200	N_2^+	Al	0.07 ± 0.02	
150	N_2^+	Al	0.03 ± 0.01	
400	N^+	Al	0.18 ± 0.05	
200	O_2^+	oxygenated Al	0.03 ± 0.01	
2000	O^+	oxygenated Al	0.26 ± 0.07	
500	O^+	oxygenated Al	0.06 ± 0.02	

[1] (Oechsner 1973)
[2] (Laegreid & Wehner 1960)

Dose-Dependent Oxygenation of Aluminum Results

When a beam of 200-eV O_2^+ or O^+ ions was incident on a clean aluminum surface, a net mass gain per incident ion was initially observed. The oxygen was obviously being embedded into the surface and near-surface bulk of the aluminum. As the total dose increased, the magnitude of the mass gain per incident ion decreased. The mass change per incident ion finally reached a constant value after the samples were exposed to a very large total dose. For the runs having large enough beam currents

(making the mass decrease measurable), the final value was negative indicating a net erosion of material per incident ion. The open squares in Figure 12 correspond to a 200-eV O^+ run that exhibited this behavior.

The aluminum sample was first cleaned with a 2-keV Ar^+ beam, as described previously. At the beginning of the run, the mass change per incident ion increased slightly from the first data point before it began the decrease toward the equilibrium condition. Implications concerning the equilibrium condition will be addressed below, but experimentally the equilibrium condition is defined as the point at which the mass change per incident ion becomes smaller than we can measure for a given run. We attribute the slightly smaller mass change per incident ion that occurred at the beginning of the run to the sputtering, i.e. negative mass change, of atoms or molecules that were weakly bound to the surface. As described above, these adsorbed atoms and molecules come from background gases in the sample chamber that stick to the surface during the time between the Ar^+ cleaning and the bombardment with the oxygen beam. This effect was observed for all runs of this type, and the magnitude of the initial increase in the mass change per incident ion observed corresponds directly to the amount of time that the adsorption of background gases occurred.

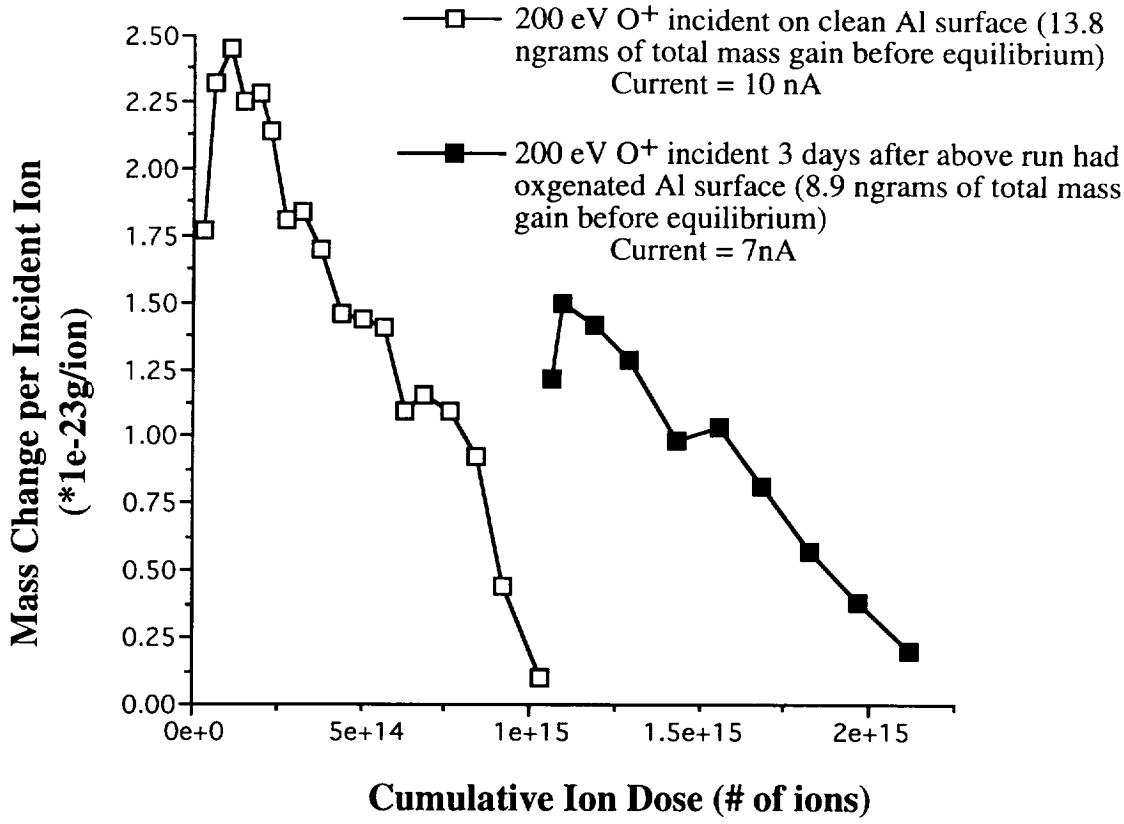

Figure 12. *Mass change per incident 200 eV O^+ ion on an aluminum surface.*

The run represented by the solid black squares in Figure 12 was performed on the same spot of aluminum that the first 200-eV O^+ run had oxygenated three days previously. The aluminum surface *was not* cleaned with argon prior to the second run. At the beginning of the second run, there was a positive mass change per incident ion that remained positive until considerably more oxygen was added to the sample.

Two additional runs were conducted in a similar fashion using 200-eV O_2^+ beams on two different aluminum samples. Unlike the procedure used for the O^+ runs, the sample surfaces were cleaned with argon before both runs. The major difference between the two O_2^+ runs was the beam current. The beam current for the run represented by the dark triangles in Figure 13 was roughly half that used for the run represented by the open triangles. As the figure shows, a positive mass increase per incident ion was observed for both runs. Furthermore, the mass changes per incident ion for the two runs are in good agreement for doses common to the two runs.

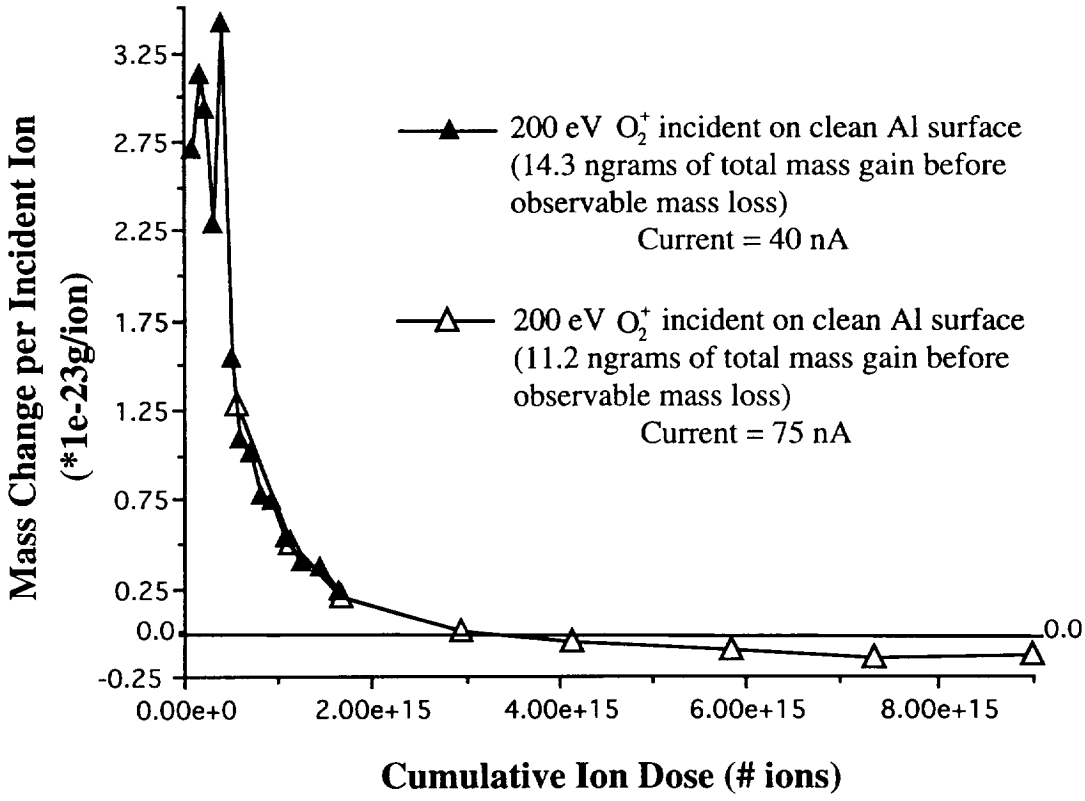

Figure 13. *Mass change per incident 200 eV O_2^+ ion on an aluminum surface.*

DISCUSSION

Dose Dependent Oxygenation of Aluminum

When a 200-eV O^+ beam was incident on the clean aluminum surface, the mass of the aluminum sample was observed to increase for a surprisingly long period of time (see the data represented by the open squares in Figure 12). The positive mass change per incident ion, which arises because the incident O^+ ions are embedded into the surface or near surface bulk, is largest for small dose. After the aluminum was exposed to the O^+ beam for a long time, i.e. large dose, the mass change per incident ion finally decreased to a value that was smaller than we could measure.

After the sample had been exposed to a large dose, an equilibrium condition was reached at which point the mass change per incident ion was constant. After the equilibrium condition was reached, the measured mass change per incident ion turned negative, it the beam current was sufficiently large. We believe that the equilibrium condition is an equilibrium between five competing processes: sputtering of the aluminum, incorporation of oxygen from the ion beam into the aluminum, sputtering of the incorporated oxygen, incorporation of oxygen from the background gas in the sample chamber, and sputtering of the adsorbed background gas atoms. The relative contributions of the five different processes are largely determined by the magnitude of the beam current.

Mass gain due to the incorporation of oxygen ceases when the surface and near-surface bulk become saturated with oxygen. For the 200-eV O^+ bombardment the total mass increase of the aluminum sample before the mass change per incident ion reached zero was 13.8 nanograms. The total mass increase of a clean aluminum sample bombarded by a 200-eV O_2^+ beam was 14.3 nanograms, which is close to the value of 13.8 nanograms measured for the O^+ run. (See Figure 13 and the accompanying description in the data section). This close agreement is also supported by other similar

runs. If we assume that no sputtering of the aluminum occurs during the period of mass increase, 14 nanograms corresponds to 11 oxygen atoms per aluminum atom in the surface layer. This is certainly not a valid assumption, but it sets a lower bound on the amount of oxygen incorporated into the aluminum, and clearly indicates that the oxygen penetrates several monolayers into the aluminum bulk.

The solid black squares in Figure 12 represent a second run made three days after the first run saturated the surface with oxygen. The sample *was not* cleaned with an Ar^+ beam before the second run. This second run is characterized by a mass gain per incident ion, with an initial value that is only about three-fifths the initial value of the gain measured during the first run. We conclude that much of the oxygen incorporated into the aluminum during the first run did not remain near the surface. The fact that the second run was able to incorporate 8.9 nanograms of oxygen into a sample which had three days before been saturated with 13.8 nanograms of oxygen reveals that ~60% of the originally incorporated oxygen had diffused out of the near-surface volume. We are not able to distinguish between diffusion of the excess oxygen deeper into the aluminum bulk and diffusion out from the surface into the vacuum.

Figure 13 shows the mass change caused by two different O_2^+ beams of the same energy but of different intensities. The beam with the smaller current permitted accurate measurements of mass change in the region of the curve corresponding to small cumulative ion doses; and the beam with the larger current allowed accurate measurements for large doses. Note that in the region of intermediate doses, the two data plots coincide. This agreement is particularly noteworthy in view of the fact that the two runs were conducted on different aluminum samples. The agreement indicates that the time scale of the oxygen diffusion is either much larger than or much smaller than the time required to acquire the data for a single run. However, if the time scale were much smaller, then the mass change per incident ion would remain constant until oxygen diffused throughout the entire aluminum sample, contrary to the data. Therefore it is probable that the time scale for diffusion is long compared to the run time. This

conclusion is supported by the 60% "refilling" of the oxygenated sample by the second 200-eV O^+ run three days after the first run.

Figures 12 and 13 reveal another interesting aspect of the oxygenation process. When the aluminum contains very little oxygen (small dose), nearly every 200-eV O^+ ion that strikes the surface is embedded in the aluminum. In contrast, approximately sixty percent of the initial 200-eV O_2^+ ions is embedded into the clean aluminum.

It is necessary for us to consider the effects of the ambient gases of the vacuum chamber. Since the pressure in the chamber increases by an order of magnitude when a beam is turned on, most of the ambient gas is from the ion source, primarily O_2 during the O^+ and O_2^+ bombardments. The influence of the ambient gas on the mass-loss measurement depends on the pressure, the sticking coefficient of the gas, and the current density of the ion beam (since this dictates the removal rate of adsorbed atoms and molecules). Below we develop a set of rate equations that describe the different processes which can either increase or decrease the mass of the sample. Note that molecular oxygen dissociates when the molecule adsorbs to the metal surface.

In order to quantitatively estimate the effects of the ambient gas, we need to know the flux and the sticking coefficient as a function of coverage. For an aluminum sample exposed to O_2 gas at room temperature, data describing the coverage, θ, as a function of L ($L = 10^{-6}$ Torr sec) can be extracted from published experiments (Hayden *et al.*, 1981 and Yu *et al.*, 1980 for example). It should be noted that, at this point, we are only discussing exposure of the aluminum surface to oxygen gas. Other than the normal thermal motion of the gas molecules, the gas is not accelerated toward the surface.

This coverage of the sample by the adsorption of gases can be described by

$$\frac{d\theta}{dt} = (1-\theta)\frac{1}{\tau} \quad \text{with initial condition} \quad \theta(t)\big|_{t=0} = 0 \tag{15}$$

when starting with a clean surface. For equation (15) and the following discussion, $1/\tau$ is the initial rate of adsorption for a clean surface. Stated differently, τ is the incident flux multiplied by the sticking coefficient which obviously makes τ dependent on the pressure

of the ambient gas. Solving equation (15), we obtain the coverage from the adsorbed gas as a function of time.

$$\theta(t) = 1 - e^{\frac{-t}{\tau}} \tag{16}$$

where θ = 1 corresponds to the saturated value. In general, $\theta(t) = \theta_0(1 - e^{\frac{-t}{\tau}})$ where θ_0 is the portion of a monolayers coverage. A value for τ can be obtained experimentally or from the literature. The information regarding the sticking coefficient as a function of coverage is included in equation (15).

If in addition to exposure to the ambient gas the sample is bombarded with an ion beam, equation (15) should contain a term that characterizes the possible removal of the adsorbed gases by the ion beam

$$\frac{d\theta}{dt} = (1-\theta)\frac{1}{\tau} - \frac{Y_1\ J}{N_0'\ q}\theta \tag{17}$$

where Y_1 is the sputtering yield for the adsorbed atoms when θ = 1, J is the current density, and N_0' is the surface density of adsorbed atoms when $\theta = 1$. If we define N_0 as the number of adsorbed atoms per unit area when $\theta = 1$, and for brevity define

$$\kappa_0 = \frac{Y_1}{N_0\ q}. \tag{18}$$

Equation (17) can then be expressed as

$$\frac{d\theta}{dt} = (1-\theta)\frac{1}{\tau} - \kappa_o\ I\ \theta. \tag{19}$$

where I is the current that strikes a unit area of the sample. The general solution to equation (19) is

$$\theta(t) = C \cdot e^{-t(1/\tau + \kappa_0 I)} + \frac{1/\tau}{1/\tau + \kappa_0 I} \tag{20}$$

where C can be determined from the initial conditions: 1) starting with a clean surface, $\theta(0) = 0$, and

$$\theta(t) = \frac{1/\tau}{(1/\tau + \kappa_0 I)} \cdot \left[1 - e^{-t(1/\tau + \kappa_0 I)}\right] \tag{21}$$

or, 2) starting with a covered surface, $\theta(0) = 1$, and

$$\theta(t) = \frac{1}{(1/\tau + \kappa_0 I)} \cdot \left[\kappa_0 I \cdot e^{-t(1/\tau + \kappa_0 I)} + 1/\tau \right]. \tag{22}$$

It is clear from equations (21) and (22) that higher beam currents will decrease the time until an equilibrium exists between the adsorption of more gas and the removal of adsorbed atoms. The coverage when this occurs will be referred to as the equilibrium coverage, θ_{eq}, and is independent of the initial conditions.

$$\theta_{eq} = \frac{1/\tau}{(1/\tau + \kappa_0 I)} \tag{23}$$

Furthermore, if $\kappa_0 I >> 1/\tau$, θ_{eq} is negligible.

Of course we are primarily interested in the coverage that arises from the ambient gas because it changes the mass of the sample. The mass change of the sample as a function of current when the sample is being bombarded by an ion beam is described by

$$\frac{dm}{dt} = m_0 \frac{dN}{dt} - m_{Al} \cdot Y_0 \cdot (1 - \theta) \cdot \frac{I}{q} \tag{24}$$

where dm/dt is the mass change of the sample occurring over the beam spot, m_0 is the mass of an adsorbed oxygen atom, m_{Al} is the mass of an aluminum atom, and Y_0 is the measured sputtering yield when $\theta = 0$ (i.e. no coverage). Formally one should include the sputtering of oxygen atoms that are embedded in the volume by the primary beam, but one can never avoid the process of filling the volume and sputtering the oxygen. Therefore we note that our measured sputtering yield values are the effective sputtering yields of aluminum when the process of sputtering embedded oxygen is included in the measurement. In equation (24), N is the number of oxygen atoms adsorbed on the surface within the beam spot area, and can be expressed as a function of the coverage

$$N(t) = N_0 \cdot \theta(t). \tag{25}$$

The first term in equation (24) describes the mass change associated with the adsorption of oxygen and the subsequent sputtering of these adsorbed atoms. The first

term can give a net positive contribution depending on the initial conditions, but is always zero when the equilibrium condition is reached. The second term describes the mass loss associated with the removal of aluminum, and is therefore always negative (because of the minus sign) for incident beam energies greater than the sputtering threshold. The second term is actually only an approximation since it suggests that the sputtering efficiency is proportional to the uncovered surface. Even for a covered surface, some sputtering of the substrate will occur, but if our experimental conditions lead to a small θ_{eq} the approximation is quite good.

We are now ready to substitute the coverage equation (either equation (21) or (22) depending on the initial conditions) into equation (24) to obtain:

$$\frac{dm}{dt} = \frac{m_0 N_0}{\tau} \cdot e^{-t\left[\frac{1}{\tau}+\kappa_0 I\right]} - \left\{\frac{m_{Al} \cdot Y_0 \cdot I}{q \cdot \left[\frac{1}{\tau}+\kappa_0 I\right]}\right\} \cdot \left\{\kappa_0 I + \frac{1}{\tau} \cdot e^{-t\left[\frac{1}{\tau}+\kappa_0 I\right]}\right\} \tag{26}$$

for the case when the surface is initially clean, $\theta(0) = 0$

or $$\frac{dm}{dt} = -m_0 N_0 \kappa_0 I \cdot e^{-t\left[\frac{1}{\tau}+\kappa_0 I\right]} - \kappa_0 I \left\{\frac{m_{Al} \cdot Y_0 \cdot I}{q \cdot \left[\frac{1}{\tau}+\kappa_0 I\right]}\right\} \cdot \left\{1 - e^{-t\left[\frac{1}{\tau}+\kappa_0 I\right]}\right\} \tag{27}$$

if the surface was initially covered, $\theta(0) = 1$.

To obtain the measured sputtering yield (Y_{meas}), we only need to normalize *dm/dt* by the mass of an aluminum atom and by the number of incident ions.

$$Y_{meas}(t) = \frac{\frac{-dm}{dt}}{m_{Al}\frac{I}{q}} \tag{28}$$

Both equation (26) and (27) reach the same equilibrium value

i.e. $$Y_{meas}(t)\big|_{t\to\infty} = Y_0 \cdot \left(1 - \theta(t)\big|_{t\to\infty}\right) = Y_0 \cdot (1 - \theta_{eq}) \tag{29}$$

The two cases, however, approach the final value from opposite directions. Figure 14, a plot of equation (26), shows that the equilibrium value is approached from above when the surface is clean at the beginning of the run.

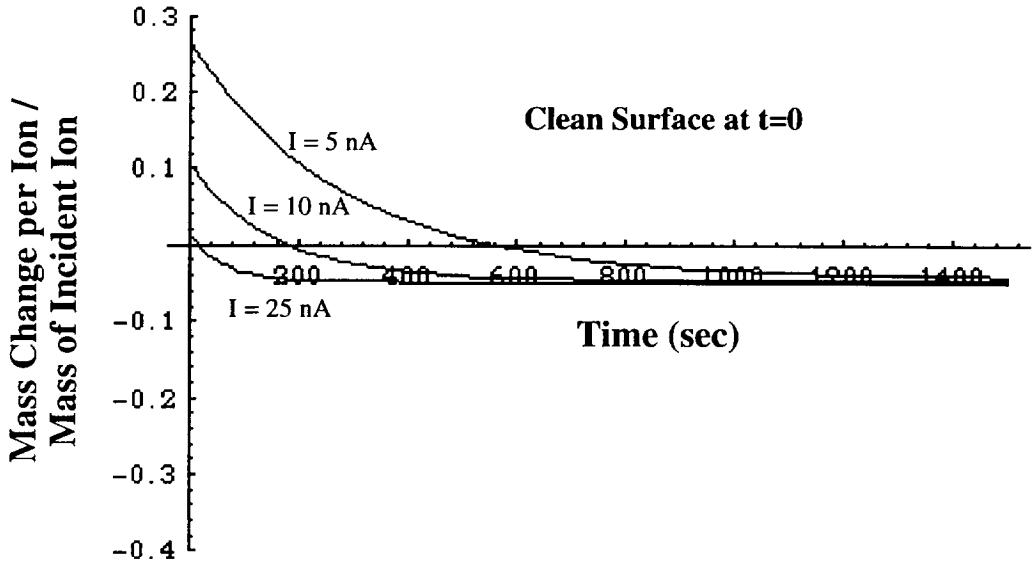

Figure 14. *Calculated mass change per incident ion as a function of bombardment time for different currents where the mass change is in units of the incident oxygen ion.*

Figure 15, a plot of equation (27), shows that the equilibrium sputtering value is approached from lower values when the surface is initially covered with adsorbed atoms. Irrespective of the initial conditions, the final measured sputtering yield at the equilibrium condition reaches the same value expressed in equation (29). We have an exponential behavior with characteristic time, t_{eff},

$$\frac{1}{t_{eff}} = \left(\frac{1}{\tau} + \kappa_0 I \right) \tag{30}$$

If we substitute the value for θ_{eq} from equation (23) into equation (29), we obtain

$$Y^{eq}_{meas} = Y_0 \cdot \left(1 - \theta_{eq}\right) = Y_0 \left(1 - \frac{\frac{1}{\tau}}{\frac{1}{\tau} + \kappa_0 I} \right) = Y_0 \frac{\kappa_0 I}{\frac{1}{\tau} + \kappa_0 I} \tag{31}$$

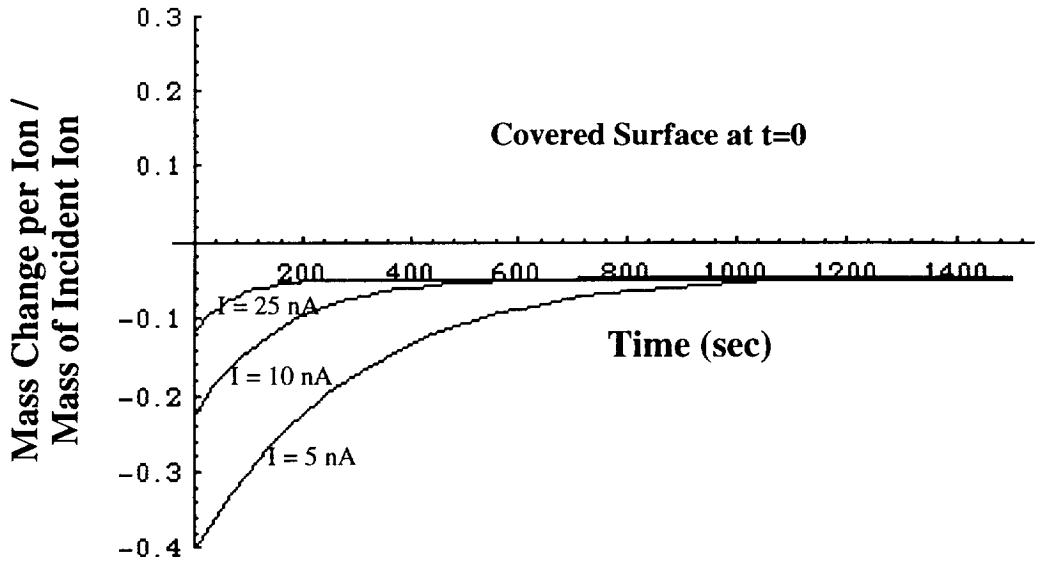

Figure 15. *Calculated mass change per incident ion as function of bombardment time for different currents where the mass change is in units of the incident oxygen ion.*

which reveals that when $\kappa_0 I >> \frac{I}{\tau}$ the final measured equilibrium sputtering yield is approximately equal to the sputtering yield of the aluminum without the effects of the ambient gas.

We are now in a position to estimate the magnitude of the effects of the ambient gas on our measurements using worst-case parameters from our experiment.

$$\kappa_0 I = \frac{Y_I I}{N_0 q} = \frac{\left(2\frac{particles}{ion}\right)\left(10^{-9}\frac{C}{\sec}\right)}{\left(4.7\cdot 10^{13} particles\right)\left(1.6\cdot 10^{-19}\frac{C}{ion}\right)} \approx \frac{1}{3800}\sec^{-1} \tag{32}$$

if the current were 1 nA. This means that a current of 1 nA removes 1/3800 of a monolayer per second. From the work of Hayden *et al.* (1981), we can ascertain that

$$\frac{1}{\tau} \approx \frac{1}{2000}\sec^{-1} \tag{33}$$

for oxygen on aluminum. This indicates that even if our currents were as low as 7 nA (the smallest current we used), then the condition $\kappa_0 I >> \frac{I}{\tau}$ is met and $Y_{meas}^{eq} \approx Y_0$

We can also calculate the time needed to effectively reach this equilibrium condition.

$$t_{eq} \approx 3\tau_{eff} = 3\left(\frac{1}{\tau} + \kappa_0 I\right)^{-1} = 3\left(\frac{1}{2000\,\mathrm{sec}} + \frac{7}{3800\,\mathrm{sec}}\right)^{-1} \approx 22 \text{ min} \qquad (34)$$

This time is much shorter than was experimentally observed before the measured mass change per incident ion reached a constant value which signaled that the equilibrium condition had been achieved. We have shown that the adsorbed gas atoms do not appreciably affect our mass loss measurements after equilibrium conditions are reached, but the above description does not explain the very long time (i.e. large dose) that was necessary before reaching the equilibrium condition. To explain this ,we need to include the process involving the dose dependent mass gain associated with the implantation of projectile ions into the aluminum. The aluminum sample obviously incorporates oxygen into the surface and near-surface bulk since we observe a fairly large mass increase of the sample before we can measure any net erosion. The aluminum sample can incorporate oxygen most efficiently when it contains the least amount of oxygen. We will now show that the implantation of projectile atoms into the bulk is responsible for the long-term effects that we measure.

To correct our rate equation for this process, we need to add the term

$$m_0 \cdot V_0 \cdot \frac{dV}{dt} \qquad (35)$$

to the right side of equation (24) where V_0 is the number of oxygen atoms implanted into the volume when the equilibrium condition is met (i.e. when volume is saturated), and V is the degree to which the volume is filled. The form of the equation that describes the rate that V changes with time is similar to the form of the coverage equation

$$\frac{dV}{dt} = (1 - V)\frac{\gamma I}{V_0 q} \qquad (36)$$

where γ is a coefficient of entrapment that represents the probability that the oxygen ions will remain trapped in the near-surface bulk when V = 0.

If the surface is initially clean, then $V(t)|_{t=0} = 0$ and the solution to equation (36) has the form

$$V(t) = 1 - e^{\left[\frac{-\gamma I t}{V_0 q}\right]}. \tag{37}$$

We then have

$$m_0 V_0 \frac{dV}{dt} = m_0 V_0 \frac{\gamma I}{V_0 q} e^{\left[\frac{-\gamma I t}{V_0 q}\right]} = \frac{m_0 \gamma I}{q} e^{\left[\frac{-\gamma I t}{V_0 q}\right]} \tag{38}$$

for the volume term which is always greater than or equal to zero. Since this term reaches zero after the equilibrium condition is achieved, it does not affect our measured equilibrium sputtering yield.

The mass change of the sample as a function of time can now be expressed if equation (38) is substituted into equation (26) if $\theta(0) = 0$ or equation (27) if $\theta(0) = 1$ i.e.

$$\frac{dm}{dt} = \frac{m_0 N_0}{\tau} \cdot e^{-t\left[\frac{1}{\tau} + \kappa_0 I\right]} - \left\{\frac{m_{Al} \cdot Y_0 \cdot I}{q \cdot \left[\frac{1}{\tau} + \kappa_0 I\right]}\right\} \cdot \left\{\kappa_0 I + \frac{1}{\tau} \cdot e^{-t\left[\frac{1}{\tau} + \kappa_0 I\right]}\right\} + \frac{m_0 \gamma I}{q} e^{\left[\frac{-\gamma I t}{V_0 q}\right]} \tag{39}$$

for the case when the surface is initially clean, $\theta(0) = 0$ or

$$\frac{dm}{dt} = -m_0 N_0 \kappa_0 I \cdot e^{-t\left[\frac{1}{\tau} + \kappa_0 I\right]} - \kappa_0 I \left\{\frac{m_{Al} \cdot Y_0 \cdot I}{q \cdot \left[\frac{1}{\tau} + \kappa_0 I\right]}\right\} \cdot \left\{1 - e^{-t\left[\frac{1}{\tau} + \kappa_0 I\right]}\right\} + \frac{m_0 \gamma I}{q} e^{\left[\frac{-\gamma I t}{V_0 q}\right]} \tag{40}$$

for the case when the surface is initially covered, $\theta(0) = 1$. A plot of equation (39) is shown in Figure 16 which agrees closely with the behavior seen in Figure 13 where a 200-eV O_2^+ beam was incident on an aluminum sample that had been cleaned with argon. The bombardment time observed in our experiment before the mass change per incident ion decreased to zero is remarkably close to the value shown by the calculated curve.

Our predictions are also quite close to the experimental observations for a surface that is initially coated before bombardment. A plot of equation (40) is shown in Figure 17 which agrees closely with the behavior seen in Figure 12 where a 10 nA, 200-eV O^+ beam was incident on an aluminum sample which had been exposed to the ambient gas for a long enough period to at least partially cover the surface. Note that the rise that

occurs in the beginning of several of the oxygenation runs is also present in the calculated plot for the surfaces that start with at least a partial coverage.

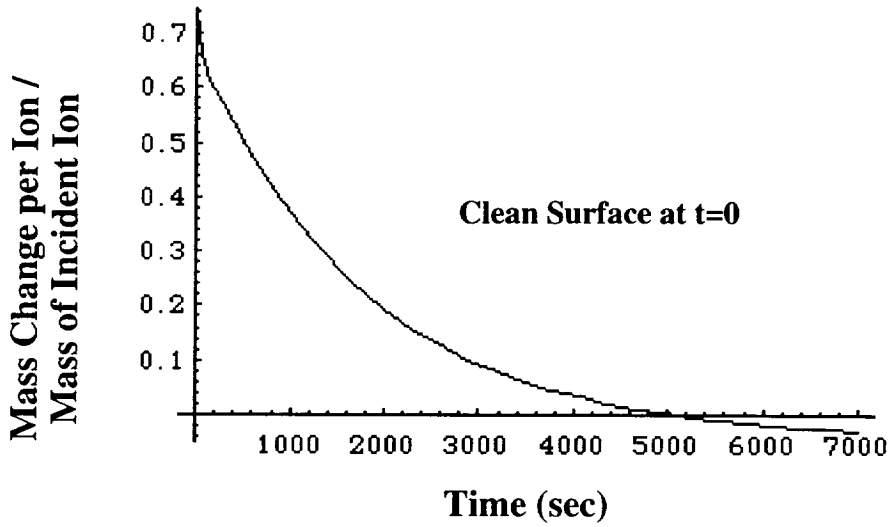

Figure 16. *Calculated mass change per incident ion for the 75 nA, 200 eV O_2^+ run as a function of bombardment time if the volume effect is included.*

We can determine a value for V_0 and γ from our data, and then use a procedure similar to the one used for equation (24) to determine the time necessary to reach the equilibrium condition for the volume process, t_{Veq}. We will show the calculation for the high current 200-eV O_2^+ run since we had enough current for that run to easily determine the time needed to reach the equilibrium condition.

$$t_{Veq} = 3\tau_{Veff} = 3\left(\frac{\gamma I}{V_0 q}\right)^{-1} = 3\left(\frac{(0.6)\,(75\cdot 10^{-9})}{(5.2\cdot 10^{14})(\,1.6\cdot 10^{-19})}\right)^{-1} \approx 1.5\ hr. \qquad (41)$$

This is nearly equal to the elapsed time observed during the experiment before the equilibrium condition was reached. A similar calculation for the low current (10 nA) 200-eV O^+ run predicts that the equilibrium time should be approximately 7 hours. This was also very close to the time observed in that experiment.

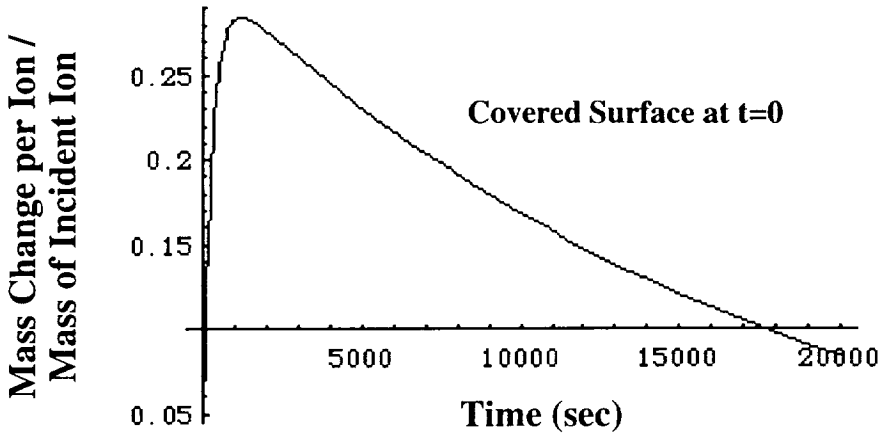

Figure 17. *Calculated mass change per incident ion for the 10 nA, 200 eV O^+ run as a function of bombardment time if the volume effect is included.*

Sputtering Yield

For the aluminum sample, the Ar^+ sputtering yields are consistently larger than those for oxygen or nitrogen ions for a given energy. For purely momentum-transfer sputtering, one would expect N_2^+ to give the highest sputtering yield because of the target-projectile mass ratio. However, other factors such as electronic interactions and chemical effects can influence the *total* sputtering yield. When the projectile species is reactive with the sample material, the chemical effects can either increase or decrease the effects of pure momentum-transfer sputtering. In chemical sputtering, energy of the projectile is first transferred to an electronic excitation of the substrate which can then impart energy to substrate particles causing their ejection from the surface. When chemical sputtering becomes an important contribution, the sputtering yield will be strongly dependent on the temperature of the sample. An increased sputtering yield is normally observed only at low energies where the effects of chemical sputtering can become more important. However if the reactivity of the bombarding species drastically increases the amount of the incident beam that remains embedded in the surface of the sample, the net sputtering yield *normally* decreases. For low energies, the decrease in sputtering yield can be attributed to two effects: 1) the altered chemical composition of

the surface layers often leading to larger effective surface binding energies, and 2) the fact that the incident particles must sputter these incorporated projectile atoms in addition to sputtering atoms from the sample material (Roth, 1983).

A comparison of the measured sputtering yield of 2-keV Ar^+ on a clean aluminum surface ($5.4x10^{-23}$ grams per incident ion) versus the sputtering yield of 2-keV Ar^+ on an oxygenated aluminum surface ($2.2x10^{-23}$ grams per incident ion) reveals that the chemical composition of the surface layers is indeed an important factor. The oxygen that is mixed with the aluminum in the surface layers likely increases the effective binding energy of the surface which leads to a smaller sputtering yield. For the 2-keV case, the altered surface layers may also affect the collisional cascade which could result in a decrease in the sputtering yield.

A decrease in the effective binding energy of the sample surface caused by the altered chemical composition of the surface layers may explain why the sputtering yields of 300- and 400-eV N_2^+ on the aluminum oxide sample are larger than the corresponding sputtering yields of O_2^+. Momentum-transfer sputtering for oxygen is favored over that for nitrogen because of the match between the projectile and target masses. Despite these considerations, the sputtering yields for nitrogen were larger than those for oxygen, indicating that the altered chemical composition of the surface layers is important in this instance.

The sputtering yield results of 2-keV Ar^+ incident on a clean aluminum surface, an oxygenated aluminum surface, and on an aluminum oxide surface are summarized in Table 6. The measured sputtering yield is largest for the pure aluminum case. It is of some surprise that the sputtering yield of argon on aluminum is approximately 40% smaller than it is for argon on aluminum oxide. A similar trend is seen from a comparison of the sputtering yields for 200-eV O_2^+ ions on an oxygenated aluminum surface to the yields for 200-eV O_2^+ ions on an aluminum oxide. The measured "equilibrium" sputtering yield of 200-eV O_2^+ on the oxygenated aluminum sample is again roughly 40% lower than the measured sputtering yield of 200-eV O_2^+ on the

aluminum oxide sample. This seems to suggest that the excess oxygen present in the oxygenated aluminum surface serves either to increase the effective binding energy on the surface or reduces the collisional cascade thus decreasing the sputtering yield.

Table 6. *Comparison of sputtering yields from 2 keV Ar^+ on similar surfaces.*

Projectile Energy	Projectile	Sample	Y (grams lost per incident ion)
2 keV	Ar^+	Al	5.4×10^{-23}
2 keV	Ar^+	oxygenated Al	2.2×10^{-23}
2 keV	Ar^+	Al_2O_3	3.7×10^{-23}

SUMMARY AND CONCLUSIONS

This report describes experiments designed to investigate the interactions of low-energy reactive ions with surfaces and measure the sputtering yields from low-energy ion beams (oxygen and nitrogen). We constructed an experimental apparatus to produce a low-energy ionic oxygen or nitrogen beam which we used to bombard aluminum and aluminum oxide samples, measuring the mass change of the sample per incident oxygen ion. A novel technique for increasing the sensitivity of a quartz-crystal microbalance by a factor of six allowed us to measure the very small mass changes induced when low-current, low-energy ion beams were incident on the thin film samples

Certain aspects of the experiment were of particular interest. For instance, when 200-eV O_2^+ or O^+ ions are incident on a clean aluminum surface, the mass of the sample increases until the surface has been exposed to a large dose of oxygen. For small O^+ dose (when the surface and near-surface bulk contain little oxygen), nearly every O^+ ion becomes embedded in the aluminum. For small O_2^+ dose, only 6 out of every 10 O_2^+ ions that strike the surface are embedded. This oxygenation process alters the chemical composition of the surface and the near-surface bulk.

One of the most striking aspects of the oxygenation process concerns the total amount of oxygen that the clean aluminum surface and near-surface bulk can hold. Our experiments revealed that the total mass increase of the aluminum is the same for bombardment by 200-eV O_2^+ or O^+ ions. We calculate that the mass increase per square centimeter of surface area is equivalent to a *minimum* of 11 oxygen atoms for every aluminum atom on the surface. A 200-eV O^+ run on an aluminum sample that had been saturated with oxygen three days earlier revealed that approximately 60% of the embedded oxygen diffuses out of the saturated volume after several days. Most of the remaining oxygen is probably in the form of Al_2O_3.

Rate equations were derived that describe the contributions of the five competing processes that change the mass of the aluminum sample during these experiments: 1) sputtering of the aluminum, 2) incorporation of oxygen from the ion beam into the aluminum, 3) sputtering of incorporated oxygen that came from the beam, 4) incorporation of oxygen from the background gas in the sample chamber, and 5) sputtering of the adsorbed background gas atoms. With these rate equations, we are able to calculate the maximum amount of incorporated oxygen and the time (for a given beam current) before the mass change per incident ion becomes a constant negative value (signifying oxygen saturation). These calculated values agree remarkably well with the experimental results.

Sputtering yield measurements were made for low-energy O^+, O_2^+, N^+, and N_2^+ on copper, aluminum, and aluminum oxide samples, and O^+ and O_2^+ on silicon oxide samples. The sputtering yields of copper under oxygen bombardment exhibited time-dependent behavior similar to that for aluminum, which is consistent with the fact that both form stable oxides. The sputtering yields for oxygen bombardment of aluminum decrease as the oxide layers form, giving the aluminum a protective coating that is more resistant to erosion. The sputtering yields measured for silicon oxide were very small, even for 2-keV oxygen beams, indicating that silicon oxide is very stable in a reactive oxygen environment.

These results will help quantify the rate that orbiting vehicles will erode when exposed to the ambient space environment. The results also suggest that the altered chemical composition of the surface that occurs plays an important role in the sputtering process, particularly for oxygen bombardment of aluminum and nitrogen bombardment of aluminum oxide.

REFERENCES

Bates, J., Gruen, D.M., and Varma, R., "Apparatus for Studies of Matrix-isolated Sputtered Products," Review of Scientific Instruments 47 (1976) 1506-10.

Brock, F.J. and Outlaw, R.A., "Orbiting Molecular-beam Laboratory," Journal of Vacuum Science 14 (1977) 1269-75.

Colligon, J.S., Hicks, C.M., and Neokleous, A.P., "Variation of the Sputtering Yield of the Gold with Ion Dose," Radiation Effects 18 (1973) 119-31

Haydon, B.E., Wyrobisch, W., Oppermann, W., Hachicha, S., Hofmann, P., and Bradshaw, A.M., "The Interaction of Oxygen with Aluminum: Mainly Ellipsometric Aspects," Surface Science 109 (1981) 207-20.

Holloway, P.H., "Quantitative Auger Electron Analysis of Homogeneous Binary Alloys: Chromium in Gold," Surface Science 66 (1977) 479-94.

Laegreid, N., and Wehner, G.K., "Sputtering Yields of Metals for Ar^+ and Ne^+ Ions with Energies from 50 to 600 eV," Journal of Applied Physics 32 (1961) 365-9.

Mecea, V.M., "A New Method of Measuring the Mass Sensitive Areas of Quartz Crystal Resonators," Journal of Physics E 22 (1989) 59-61.

Oechsner, H. "Sputtering of Polycrystalline Metal Surfaces of Oblique Ion Bombardment in the 1 keV Range," Zeitschrift für Physik 261 (1973) 37-58.

Oliva-Florio, A., Baragiola, R.A., Jakas, M.M., Alonso, E.V., and Ferrón, J., "Noble-gas Sputtering of Gold and Copper: Dependence on the Energy and Angle of Incidence of the Projectiles," Physical Review B 35 (1987) 2198-204.

Robinson, M.T., and Southern, A.L., "Sputtering Experiments with 1- to 5-keV Ar^+ Ions II. Monocrystalline Targets of Al, Cu, and Au," Journal of Applied Physics 38 (1967) 2969-73.

Roth, J., "Chemical Sputtering," in *Sputtering by Particle Bombardment II: Sputtering of Alloys and Compounds, Electron and Neutron Sputtering, Surface Topography*, ed. Behrisch, R. (Springer-Verlag, New York, 1983) 91-146.

Sauerbrey, G.Z., "Use of Vibrating Quartz for Thin Films Weighing and Microweighing," Zeitschrift für Physik 178 (1959) 206-22.

Sigmund, P., "Sputtering by Ion Bombardment: Theoretical Concepts," in *Sputtering by Particle Bombardment I: Physical Sputtering of Single-Element Solids*, ed. Behrisch, R. (Springer-Verlag, New York, 1981) 9-67.

Ullevig, D.M., and Evans, J.F., "Measurement of Sputtering Yields and Ion Beam Damage to Organic Thin Films with the Quartz-crystal microbalance," Analytical Chemistry 52 (1980) 1467-73.

Ullevig, D.M., Evans, J.F., and Albrecht, G., "Effects of Stressed Materials on the Radial Sensitivity Function of a Quartz-crystal microbalance," Analytical Chemistry 54 (1982) 2341-1.

Ward, M.D and Delawski, E.J., "Radial Mass Sensitivity of the Quartz-crystal microbalance in Liquid Media," Analytical Chemistry 63 (1991) 886-90.

Wimmer, L., Hertl, S., Hemetsberger, J., and Benes, E., "New Method of Measuring Vibration Amplitudes of Quartz Crystals," Review of Scientific Instruments 55 (1984) 605-9.

Yu, H.L., Muñoz, M.C., and Soria, F., "On the Initial Stages of Oxidation of Al(111) by LEED Analysis," Surface Science Letters 94 (1980) L184-90.